



Regular Article

Optimization and photomodification of extremely broadband optical response of plasmonic core-shell obscurants



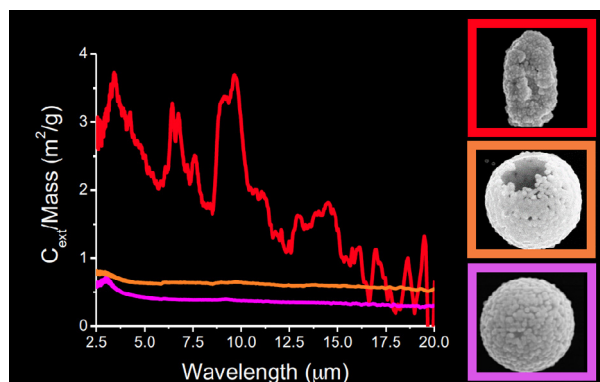
Vashista C. de Silva^a, Piotr Nyga^b, Vladimir P. Drachev^{a,c,*}

^aUniversity of North Texas, Department of Physics and Advanced Materials & Manufacturing Institute, 1155 Union Circle, Denton, TX 76203, USA

^bMilitary University of Technology, Institute of Optoelectronics, 2 Kaliskiego Str., 00-908 Warsaw, Poland

^cSkolkovo Institute of Science and Technology, 3 Nobel St., Moscow 143026, Russia

GRAPHICAL ABSTRACT



ARTICLE INFO

Article history:

Received 11 July 2016

Revised 18 August 2016

Accepted 18 August 2016

Available online 26 August 2016

Keywords:

Broadband absorption

Nanoparticle

Nobel metal

Silica

Mass extinction coefficient

Photomodification

Plasmonic

Core-shell

Obscurants

ABSTRACT

Plasmonic resonances of the metallic shells depend on their nanostructure and geometry of the core, which can be optimized for the broadband extinction normalized by mass. The fractal nanostructures can provide a broadband extinction. It allows as well for a laser photoburning of holes in the extinction spectra and consequently windows of transparency in a controlled manner. The studied core-shell microparticles synthesized using colloidal chemistry consist of gold fractal nanostructures grown on precipitated calcium carbonate (PCC) microparticles or silica (SiO₂) microspheres. The optimization includes different core sizes and shapes, and shell nanostructures. It shows that the rich surface of the PCC flakes is the best core for the fractal shells providing the highest mass normalized extinction over the extremely broad spectral range. The mass normalized extinction cross section up to 3 m²/g has been demonstrated in the broad spectral range from the visible to mid-infrared. Essentially, the broadband response is a characteristic feature of each core-shell microparticle in contrast to a combination of several structures resonant at different wavelengths, for example nanorods with different aspect ratios. The photomodification at an IR wavelength makes the window of transparency at the longer wavelength side.

© 2016 Elsevier Inc. All rights reserved.

1. Introduction

Optical properties of metallic nanoparticles can be controlled by their composition, size and shape. Nanoparticles dispersible in liquids or air, showing strong scattering and/or absorption, are of interest for many applications including obscurants [1], photothermal

* Corresponding author at: University of North Texas, Department of Physics and Advanced Materials & Manufacturing Institute, 1155 Union Circle, Denton, TX 76203, USA.

E-mail addresses: vashistadesilva@my.unt.edu (V.C. de Silva), piotr.nyga@wat.edu.pl (P. Nyga), vladimir.drachev@unt.edu (V.P. Drachev).

therapy [2], enhanced biomedical imaging [2], photon-heat conversion based energy harvesting [3], and sensing [4]. Depending on the application, specific optical properties and spectral bandwidth are required. Most of the applications rely on optical properties in the visible and the near-infrared. Some, like photothermal therapy and photon-heat conversion, require strong absorption. For others like biomedical imaging, strong scattering is important.

In order to use particles as efficient obscurants the extinction normalized by mass should be high in the broad spectral range and characterized by the mass extinction coefficient (MEC, m^2/g). These airborne particles can obscure some parts of the electromagnetic (EM) spectrum by attenuating the transmission of electromagnetic waves through scattering or absorption. The existing obscurants are typically appropriate either for the visible or infrared range, meaning that one has to use a set of different types of obscurants to cover all, visible, near-IR, mid-IR, and far-IR ranges. For the visible spectrum the hexachloroethane, alkali halide and phosphorus-derived smokes are commonly used [5–11]. The MEC of such smokes in the visible spectral range is of the order of 2–5 m^2/g [8,9], but it substantially decreases with wavelength [6,8–10]. In addition these smokes are potentially toxic [11]. An example of non-toxic visible obscurants are nanometer size titanium dioxide (TiO_2) [9,12–14] or silicon dioxide (SiO_2) [14] powders. Measured MEC of titanium dioxide reaches about 4 m^2/g [9,13]. However, their obscuring properties are very limited in infrared, since the scattering strongly decreases as the wavelength increases. For the infrared, graphite and various metals flakes have been experimentally tested as candidates for obscurants. Some of the materials, like brass, are toxic [15] and, some, like graphite based materials are flammable [16]. Calculations show that metallic fibers with few micrometers length and diameter of the order of 50–100 nm could give high MEC in the narrow band in the IR. Silver fibers in isopropanol show MEC of up to 20 m^2/g at 5 μm [17,18]. Note that these high aspect ratio metal fibers are hardly keeping their properties if suspended in air due to their mechanical instability and sensitivity of the optical response to the geometry of individual fiber and their agglomeration.

It is beneficial for the obscurant applications to have aerosol with high extinction at low mass in a spectral range covering visible, near-mid-far-IR, which would be considered as extremely broadband in this case. Such an extremely broadband response is typical for fractal planar films of Au or Ag [19–24]. These fractals in solutions or in planar films enable a photoburning of the spectral holes in the visible and near-IR [25,26] and far-IR [27,28]. A preset spectral window of transparency is another desirable feature of the obscurants.

Submicron particles can be simultaneously an aerosol and a good platform for the fractal metal nanostructures. The resonant narrow-band optical response [29–32] or broadband 0.5–1 μm [33] response of the core-shell particles depends on the shell nanostructure.

Recently we have shown that the extremely broadband extinction (0.5–20 μm) of the metallic fractal nanostructures is caused mainly by the absorption if grown on a sphere, in contrast to the planar fractal films, where the absorption and reflection equally contribute to the extinction [34].

Here we optimize obscurants made of core-shell submicron particles, each of which is covering this spectral range from the visible to IR. It allows as well for a laser photoburning of holes in the extinction spectra and consequently making windows of transparency in a controlled manner. The photomodification at an IR wavelength makes window of transparency at the longer wavelength side. The core-shell nanoparticles have been synthesized using colloidal chemistry and consist of gold fractal nanostructures grown on precipitated calcium carbonate (PCC) microparticles or silica (SiO_2) microspheres. The experiments show that the rich

surface of the PCC flakes is the best core for the fractal shells providing the highest mass normalized extinction over the extremely broad spectral range. The mass normalized extinction cross section up to 3 m^2/g has been demonstrated in the broad spectral range from the visible to mid-infrared. The broadband response is a characteristic feature of each core-shell microparticle. It should be emphasized that this broadband response is not due different types of core-shells, but rather from the same. This is in contrast to, for example nanorods, which can also provide a broadband response, but due to different aspect ratios.

2. Methods and materials

2.1. Synthesis of Au/SiO₂ microspheres

Silica microspheres (Bangs Lab) with diameters of about 0.5 μm , 0.8 μm , 1.8 μm and 4.5 μm were coated with gold nanostructures using a modified method of the reduction of gold salt, chloroauric acid (HAuCl_4) with formaldehyde (CH_2O) in the presence of surfactants and stabilizers. The reduction method was initially developed for continuous shells [35,36], where the silica surface must be seeded with gold nanoparticles prior to shell growth. The seeding step was omitted in our experiments and the chemicals concentrations were adjusted.

2.1.1. Synthesis of semicontinuous core-shell

In order to fabricate semicontinuous shells, gold was directly synthesized on the amino functionalized silica microspheres. The surface coverage of the gold on the microsphere surface was varied for different samples by varying the reduction time. Specifically, 30 mg of potassium carbonate (K_2CO_3) was dissolved in 100 mL of ultra-pure water. The solution was stirred for 10 min, and 300 μL of 50 mM HAuCl_4 was added into the solution. Next, amine functionalized silica microspheres followed by 40 μL of 0.36 mM CH_2O were added to the vigorously stirred solution. After the growth of the gold shells, the shell surface was stabilized with polyvinylpyrrolidone (PVP) to prevent aggregation of the microspheres. Finally, the solution was centrifuged to collect gold-coated silica microspheres and remove the residual reagents. Collected particles were re-dispersed in ultra-pure water and centrifuged a few times.

2.1.2. Synthesis of coreless fractal shells

Synthesis of coreless fractal shells were made by etching away the silica core of our standard core-shell colloid. This was done using buffered hydrofluoric acid (BHF), which is a SiO_2 etchant. Fabricated core-shell structures were submerged in the BHF solution for 5–10 min. Then the particles were separated by washing with ultrapure water several times.

2.1.3. Synthesis of Au fractal shells on precipitated calcium carbonate (PCC)

Synthesis of Au fractal shell on PCC was slightly modified relative to the Au-SiO₂ procedure. The PCC surface was functionalized with 3-aminopropyltriethoxysilane (APTES), silane groups were attached to the surface and left the amino groups outside the surface. To accomplish this, 5.2 mg (in average 4.5×10^{11}) of PCC particles (~ 700 nm median size) was suspended in 50 mL absolute ethanol and stirred for 30 min at a rate of 1000 rpm. Then 50 μL of 0.21 μmol APTES was added drop wise and the solution stirred for 12 h. Two components were then separated after stirring. The heavier component, APTES coated PCC, were in the lower part, as they precipitated to the bottom. The solution was refluxed for one more hour to ensure the amino groups bonded to the PCC

surface as covalent bonds. These particles were centrifuged several times in order to remove the residues. The Au reduction was performed by chloroauric acid (HAuCl₄) with formaldehyde (CH₂O). During the reduction reaction an Au nanoparticles fractal structure was formed on the amino group modified surface of the PCC particles. Negatively charged gold nanoparticles were attached to positively charged amino groups and kept growing gold around each gold nanoparticle until stabilizer (PVP) was added, stabilizing gold shells around the PCC nanoparticles. Gold coverage in the shells was controlled by varying the PCC concentration and reduction time. PCC was obtained from Specialty Minerals. The chemicals, PVP, HAuCl₄, K₂CO₃, and CH₂O were purchased from Sigma-Aldrich.

2.2. Electron microscopy

The field emission scanning electron microscope (FESEM) images provide the structural characterization of the samples. Consequent analysis gives the fractal dimension, particles mean size, and the particle surface density. The shells have the fractal structure with fractal dimension $D = 1.75\text{--}1.82$. It was calculated as the power dependence of the number of gold nanoparticles N_p inside the circle of radius R , $N_p/N_0 = (R/R_0)^D$, where N_0 is the number of nanoparticles in a small reference circle of radius R_0 .

2.3. Optical spectroscopy

The synthesized gold-coated microspheres were deposited as a sub-monolayer on zinc selenide (ZnSe) substrates for the infrared spectroscopy and on fused silica substrates for spectroscopy in the visible range. A drop-and-dry method was used for highly uniform distribution. The ultra-violet-visible (UV-vis) and infrared (IR) extinction spectra were collected using UV-vis -near-IR and FTIR spectrometers and normalized by the particles surface density (particles per μm^2).

2.4. Extinction cross-section

The extinction cross section (a quantity with dimensions of area), C_{ext} , is defined in Eq. (1) below as the intensity change in the incident beam under transmission through a single layer of particles.

$$\Delta I = -I_0 C_{\text{ext}} N_V \Delta l = -I_0 C_{\text{ext}} N_S \quad (1)$$

where I_0 is the incident intensity, Δl is a hypothetical thickness of a single layer of particles, N_V and N_S are the particle volume density and surface density respectively. Mass normalized extinction is given as

$$C_{\text{ext}}/m_p = -\frac{\Delta I}{I_0 N_S m_p} = \frac{1-T}{N_S m_p} [\text{m}^2/\text{g}], \quad (2)$$

where $m_p = \rho V_p$ (material density times particle volume) is the average mass of a particle. Here, N_S has been estimated from FESEM images, and average particle mass using known particle density and calculated particle mass. Particle mass was calculated by using known material density and volume of the particle. The second approach is expressed in Eq. (3), with the known total mass in the spot, area of the central and edge parts of the spot, and particle coverage at the center and edge of the spot.

$$C_{\text{ext}}/m_p = \frac{1-T}{M} \left[S_c + S_e \frac{f_e}{f_c} \right] [\text{m}^2/\text{g}] \quad (3)$$

Total particle mass in the spot, M is calculated following Eq. (4), where S_c , S_e and f_c , f_e are respectively surface areas of the center and edge, and fractions of the center and edge.

$$M = \int_0^R M_s(r) 2\pi r dr \approx M_s(\text{center}) S_c + M_s(\text{edge}) S_e \quad (4)$$

Here M_s is given by Eq. (5).

$$N_S m_p = M_s(\text{center}) = M \left[S_c + S_e \frac{f_e}{f_c} \right]^{-1} \quad (5)$$

Thus one can use two ways to perform the mass normalization after measurements of the transmission spectra T , based on Eqs. (2) or (3). In the first case the particle surface density N_S has to be estimated from FESEM images, and average particle mass must be calculated from known particle density and measured mass density. The second approach (Eq. (3)) implies measurements of the total mass in the spot, area of the central and edge parts of the spot, and particle coverage at the center and at the edge. To deposit a priori known mass in the spot a water or ethanol solution with known mass of particles is prepared. This solution is then deposited in a small volume on a substrate. A very uniform distribution of particles can be obtained on both the ZnSe and glass substrates. The radial dependence and consequently total mass is measured typically out of about 20 images.

2.5. Laser photomodification

The laser used for photomodification studies was a 10.6 μm pulsed MTL-3GT Mini TEA CO₂ laser (Edinburgh Instruments Ltd.). The laser radiation was linearly polarized and the pulse duration was 50 ns.

3. Results and discussion

Several different core-shell structures have been studied, all are based on dielectric core and fractal gold shell. The shell optical properties are influenced by the surface plasmon resonances (SPRs), which are collective oscillations of electrons in a metal-dielectric composite that are excited by an electromagnetic wave. Resonances in a broad spectral range are supported by the localized plasmon modes. A variety of these modes coexists due to fractal geometry of the metal nanostructures [19,20,37,38]. The extremely broadband spectrum extends from the near ultraviolet to the mid-infrared (0.3–20 μm). In order to cover the long wavelength side of this range the geometry should allow to place enough nanoparticles providing long chain supporting the plasmon modes. This requirement is easy to satisfy in case of plane films but makes not obvious selection of the core diameter or characteristic size. The optimization of mass extinction cross-section was performed for different diameters of the silica core and complex shape PCC microparticles.

3.1. Silica - gold core-shell microparticles

A number of silica-gold core-shell structures with different core diameters was synthesized as a first step of optimization. Fig. 1 shows the mass normalized extinction cross-section spectra of the core-shell microparticles in the VIS - near-IR (A) and mid-IR - far-IR spectral ranges (B).

FESEM images of the core-shell nanostructures with different core size are shown in Fig. 2 corresponding to the MEC spectra in Fig. 1.

Core-shell structures in Fig. 2 have shell thickness of about 70–90 nm with core diameters ranging from 0.5 μm to 4.5 μm with all the parameters shown in Table 1. The 0.5 μm silica particles have different uncompleted shells. Isolated Au nanoparticles are randomly distributed on the core surface. The core-shell structures are labeled as per core diameter: 4.5 μm - green, 1.8 μm - red,

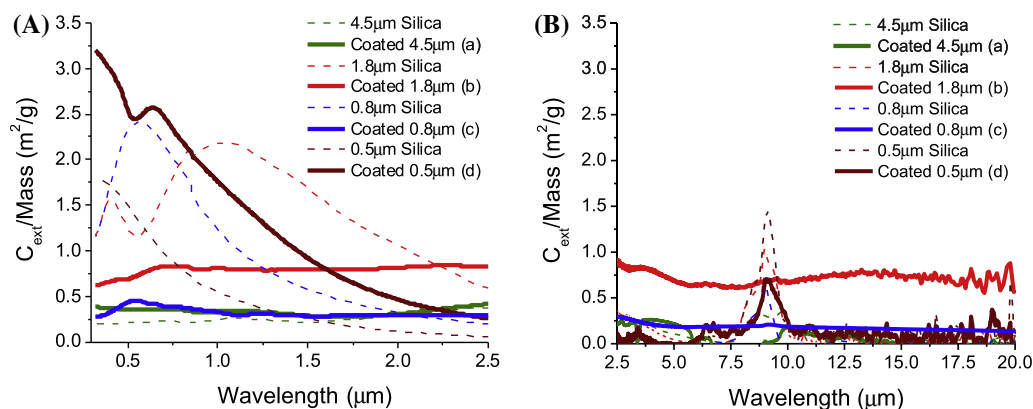


Fig. 1. Mass normalized extinction cross-section spectra in the VIS - near-IR (A) and mid-IR - far-IR spectral ranges (B) for the gold coated SiO₂ microspheres - solid lines and for the bare SiO₂ microspheres - dashed lines (core diameters in μm : 4.5-green, 1.8-red, 0.8-blue, and 0.5-brown). (For interpretation of the references to colour in this figure legend, the reader is referred to the web version of this article.)

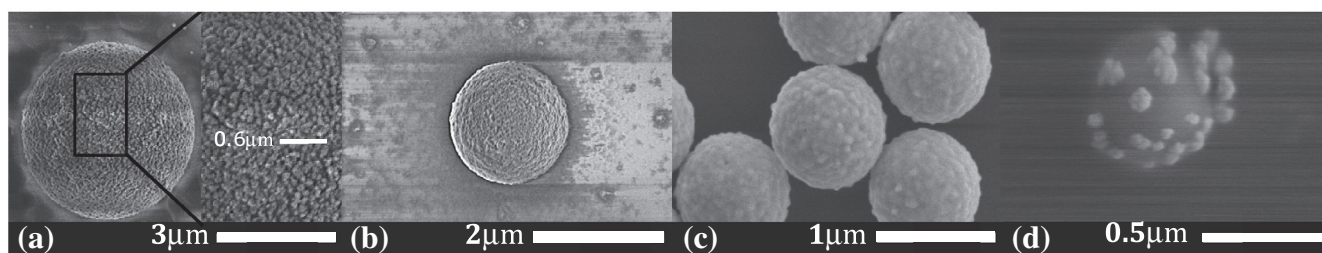


Fig. 2. FESEM images of gold coated SiO₂ microspheres (core diameters in μm : 4.5 (a), 1.8 (b), 0.8 (c), and 0.5 (d)).

Table 1

Calculated experimental parameters of samples shown in Fig. 2(a-d).

	(a)	(b)	(c)	(d)
Shell thickness (nm)	89	73	67	70 ^a
Total diameter (nm)	4532 ± 74	1860 ± 20	920 ± 10	579 ± 11
Density (μm^{-2})	0.008 ± 0.001	0.055 ± 0.01	0.50 ± 0.02	0.60 ± 0.06
Mass shell (g)	1.0E-10	1.4E-11	2.3E-12	1.2E-13
Mass core (g)	8.7E-11	5.3E-12	5.0E-13	8.2E-14
Mass total (g) per microsphere	1.9E-10	1.9E-11	2.8E-12	2.0E-13

^a Gold is synthesized as isolated particles, and each nanoparticle has mean diameter of about 70 nm. Coverage of Au particles on the silica sphere is 0.1. Shell Mass of sample (d) is calculated by multiplying shell volume by coverage times gold density. Au density = 19 g/cm³, SiO₂ density = 2 g/cm³.

0.8 μm - blue, and 0.5 μm - brown. Fig. 1 shows strong extinction for 0.5 μm sample in the visible and others show broadband extinction from visible to mid-infrared. The small core-shells (0.5 μm) show spectra corresponding to the combined plasmon resonance of the isolated gold nanoparticles and bare silica microsphere. The other three samples show optimum in the MEC for the 1.8 μm core-shells. Qualitatively it can be understood from the following. Indeed, in order to cover a broad band and specifically long wavelength side the circumference of the surface should allow to place enough nanoparticles providing long chain supporting the plasmon modes. This point makes the larger diameter to be preferable for the broadband response. Some kind of saturation of the response versus diameter can be expected though. However, increasing the core-shell diameter tends to increase the mass of the shell and core, which explains the highest MEC for a middle size core-shell.

The results in Fig. 3 with corresponding images in Fig. 4 show effect of the different gold coverage on the core-shell performance for silica core diameter 0.8 μm (see all the parameters in Table 2). Fig. 3 shows that the mass normalized extinction tends to extend over the visible and infrared ranges with increasing the Au shell

coverage. The bare SiO₂ particles show reasonably high extinction in the visible spectral range resulting from scattering which decreases as the spectrum proceeds to the infrared, except at 9 μm due to the vibrational stretching band of SiO₂ [39]. Au fractal film on SiO₂ substantially enhances the extinction of particles in IR spectral range due to the resonant conditions in the Au fractal shell and at the same time the visible extinction stays at reasonable level.

It shows that 1 m²/g obtained with 1.8 μm microspheres the mass normalized extinction from visible to infrared spectrum is what can be achieved with core-shell spherical microspheres.

3.2. Coreless gold shell microspheres

Obviously the coreless shells should improve the mass normalized extinction if the shell extinction is not affected by the core removal. Coreless structures were made by etching away the silica core in the samples fabricated as described in the methods. A representative Au shell on silica core and coreless Au shell are presented in Fig. 5B and C, respectively. Through the hole, missing shell part, it is visible that the core-less structure was achieved. The gold shell after core etching preserves its shape and morphology

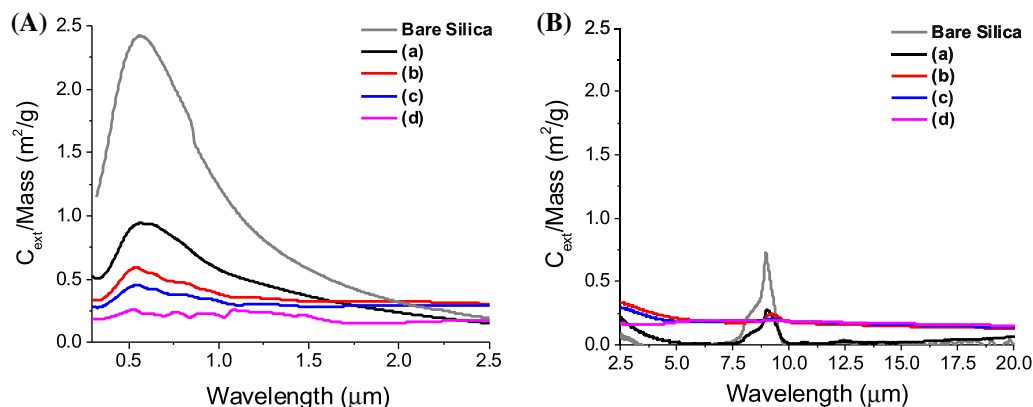


Fig. 3. Mass normalized extinction cross-section spectra in the VIS - near-IR (A) and mid-IR - far-IR spectral ranges (B) for gold coated SiO₂ microspheres (core diameter 0.8 μm with different gold shell coverage).

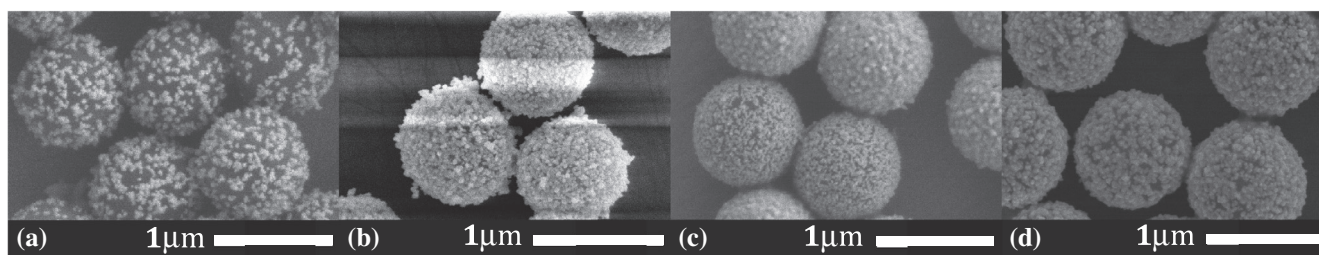


Fig. 4. FESEM images of gold coated SiO₂ microspheres (core diameter 0.8 μm with different gold shell coverage).

Table 2

Calculated experimental parameters of samples shown in Fig. 4(a-d).

	(a)	(b)	(c)	(d)
Shell thickness (nm)	43	63	67	67
Total diameter (nm)	870 ± 20	910 ± 10	920 ± 10	920 ± 10
Density (μm ⁻²)	0.63 ± 0.07	0.66 ± 0.02	0.57 ± 0.02	0.50 ± 0.02
Shell mass (g)	6.80E-13	1.30E-12	1.60E-12	2.30E-12
Core mass (g)	5.05E-13	5.05E-13	5.05E-13	5.05E-13
Total mass (g) per microsphere	1.18E-12	1.80E-12	2.10E-12	2.80E-12

Au density = 19 g/cm³, SiO₂ density = 2 g/cm³.

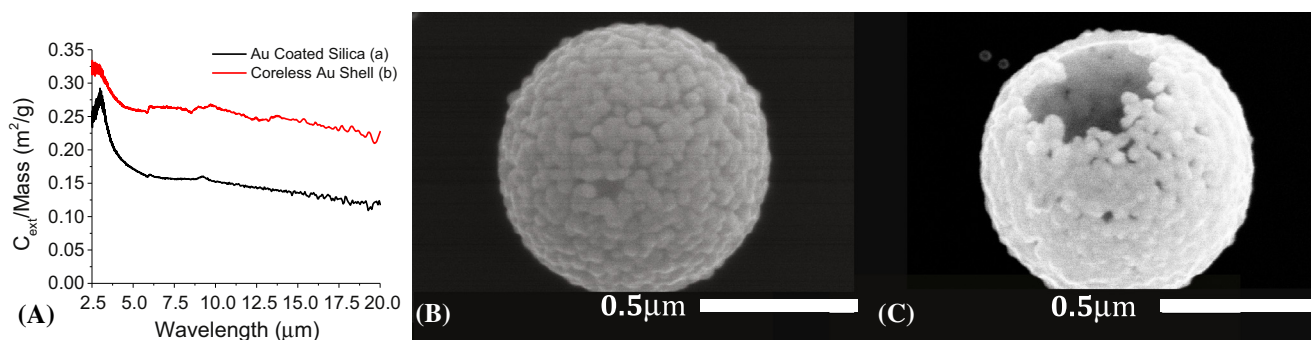


Fig. 5. (A) Mass normalized extinction spectra of gold coated SiO₂ and coreless microspheres. FESEM image of the gold coated SiO₂ (B) and coreless (C) microspheres (core diameter is about 0.8 μm).

for majority of the structures. It is stable in solution and on a substrate. Of course, it preserves the shape as long as one does not apply any external force.

The extinction of coreless particles normalized per mass (Fig. 5A) is increased as expected, confirming that the shell extinc-

tion holds after etching. Coreless structure's mass (2E-12 g) is lower as compared to core-shell structure (2.6E-12 g). The vibrational stretching band of SiO₂ [39] at 9 μm, which is slightly visible for particles with silica core, does not show up for the coreless structures.

3.3. Gold fractals on precipitated calcium carbonate

The goal of this part of experiments was to study the effect of the core shape, like flakes on the obscurants' performance. In addition, the PCC material has lower density, 0.53 g/cm^3 instead of 2 g/cm^3 for silica. Due to higher refractive index 1.65 [40] and high-opacity [41] the PCC can be a good substrate for the fractal shell. As it was mentioned the synthesis includes one more step to modify the surface with amino groups prior to the Au shell reduction. One can see in Fig. 6 that the performances of these structures through the broadband spectral range ($0.3\text{--}20 \mu\text{m}$) is very good.

In order to perform the mass normalization procedure for the PCC particles, one has to provide uniform deposition of the particles on a substrate. The mass normalization in the PCC case was a challenge due to significant variation in the shape and size of the bare particles. Spectra in Fig. 6 show increase in mass normalized extinction cross-section as the gold reduction time increases and consequently the fractal shell becomes more rich and increases in mass.

FESEM images in Fig. 7 show sufficient fractal like Au coverage on the randomly shaped and sized PCC. As previously discussed regarding mass normalization, the uniformity and distribution of PCC on the substrate should be significant to satisfy Eq. (3). Mass of individual PCC particles, calculated using the average size of the particle and its density, is $2.3 \times 10^{-14} \text{ g}$ (Table 3). The average size of PCC was measured by analyzing about 50 PCC particles. The spectra of Au-coated PCC particles in Fig. 6 show that the extinction extends over the visible and infrared ranges. The extinction of bare PCC particles shows reasonably high extinction in the visible spectral range due to the strong scattering and decreases as spectra proceeds to infrared. Au fractal film on PCC greatly enhances the extinction in both visible and IR spectral range due to the resonant conditions in the Au fractal shell and scattering of PCC.

Note that the increase in the MEC for PCC fractal shells by factor 4.7 in the VIS-mid-IR is due to material density ratio 3.3 and the rest caused by the shape effect.

3.4. Photomodification of broadband response in infrared of the fractal core-shells

Laser induced changes in structure and optical properties of metallic nanospheres [42], nanorods [43–45] and core-shell spheres with uniform shells [46,47] have been extensively studied in UV, VIS and near-IR. However, no studies in the mid-IR were performed for the fractal core shells with a broad band extinction. The

high, broadband extinction of studied core-shell structures can be used as a basis for the development of efficient optical obscurants with preset windows of transparency within a broad spectral range through photomodification of the nanoscale morphology of the fractal metal shell on dielectric core.

Modification of the local nanostructure of fractal metal film can be accomplished using laser pulse light-induced changes due to the coalescence or ablation of the nanostructures. A relatively high-intensity incident pulse can excite resonant responses in the metal nanostructure. If the accumulated energy in a local volume of the resonant mode reaches a threshold value, sufficient heating occurs to restructure the metal in the area. The structure of the resonant mode is thereby modified, and the modified volume no longer absorbs at the incident laser wavelength. One specific feature, predicted for the IR photomodification for planar films and confirmed in experiments [27,28] is that the absorption at wavelengths longer than the laser wavelength can be greatly decreased as a result of the photomodification process. We found similar behavior for the fractal shells.

The selective photomodification of core-shell extinction was performed for the Au fractal shells formed on silica microspheres. In the experiments, core-shell particles were deposited on ZnSe substrates, which are appropriate for spectroscopic analysis and photomodification experiments in the IR.

Photomodification was done using CO_2 laser operating at $10.6 \mu\text{m}$ and generating 50 ns pulses. The photoburning experiment was performed using one pulse photomodification with linear vertical polarization and next pulse with orthogonal polarization at the same location on the sample. Thus the cross-polarized photomodification can be performed and then probed after each pulse by polarization controlled FTIR spectrometer at two orthogonal linear polarizations.

First, in the spectral-burning experiment Au-coated $0.8 \mu\text{m}$ silica microspheres were photomodified by a single laser pulse with linear polarization. The pulse energy density ($1/e^2$) was 150 mJ cm^{-2} .

Fig. 8B shows noticeable changes in the structure of core-shells after photomodification as compared to the original structure (Fig. 8A). There are spherical Au particles with $100\text{--}150 \text{ nm}$ diameter present on the SiO_2 cores, probably due to the coalescence of resonant fractal structures. The spectra in Fig. 9A show the initial extinction of core-shell particles (normalized to ZnSe substrate) and the extinction after photoburning. The photomodification process results in decrease of the extinction for wavelengths longer than about $4 \mu\text{m}$, creating long-pass filters. This effect can be clearly seen in Fig. 9B, where relative changes in extinction are

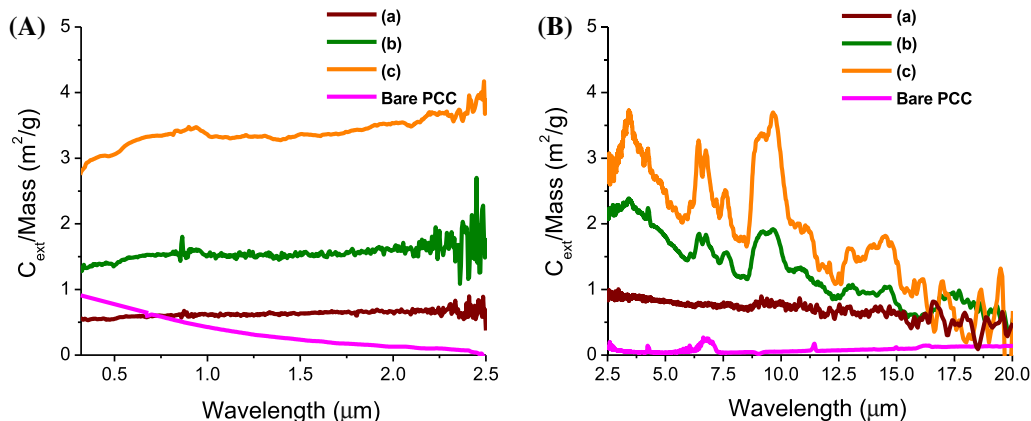


Fig. 6. Mass normalized extinction cross-section spectra in the VIS - near-IR (A) and mid-IR - far-IR spectral ranges (B) for gold-coated PCC and bare PCC particles. The reduction time is gradually increased: (a) 1.5 h, (b) 3.5 h, and (c) 48.5 h.

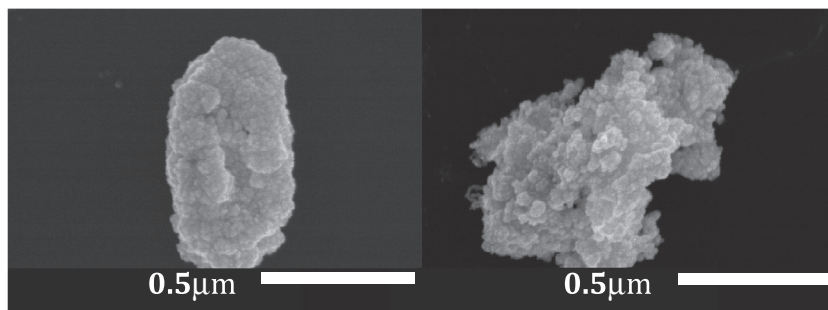


Fig. 7. FESEM images of representative Au coated PCC of the size $\sim 0.7 \mu\text{m}$ and illustrates how the Au structure is formed on PCC.

Table 3

Calculated experimental parameters of PCC samples. The samples (a), (b), and (c), correspond to the spectra (a), (b), and (c) shown in Fig. 6.

	(a)	(b)	(c)
PCC Particle surface density (μm^{-2})	0.28 ± 0.04	0.16 ± 0.02	0.08 ± 0.01

Average mass core = $2.3\text{E}-14 \text{ g}$, average mass shell = $7.2\text{E}-13 \text{ g}$, Mass total per PCC = $7.4\text{E}-13 \text{ g}$, PCC density = 0.53 g/cm^3 .

presented. The changes in extinction are nearly independent on the probe beam polarization.

Surprisingly, there is no polarization selectivity here even though the spectral selectivity clearly manifests itself, as shown in Fig. 9A and B for the normalized relative changes in the extinction spectra. We see that an incident laser pulse of a certain linear polarization (vertical in this case) results in almost the same spectral changes for both the vertical and horizontal polarizations of the probe light in the FTIR measurements. The corresponding structural changes of the shell's metal nanostructure are very different for different particles, as can be seen in Fig. 8a and b.

Next, photomodification with a second pulse was performed, this time with the orthogonal linear polarization as compared to the first pulse. The same area of sample was illuminated. Thus Au shells were photomodified with cross polarized pulses. The energy density for this particular photomodification was 150 mJ cm^{-2} .

After cross-polarized photomodification the extinction decreases further (Fig. 10A) for wavelengths longer than $4 \mu\text{m}$ and barely changes for shorter wavelengths. The relative change in extinction saturates for the wavelengths longer than the laser wavelength (Fig. 10B). The observed decrease in extinction is stronger than that for the single pulse photomodification as presented in Fig. 9.

It is important to emphasize the following points concerning the polarization dependences.

- Before the photomodification the spectra collected with two orthogonal polarizations are the same since, indeed, there is no any preferable direction in average.
- However, the linear polarization of the laser light used for photoburning potentially can introduce the anisotropy. Surprisingly there is only minor difference for the spectra at two orthogonal polarizations of probe. This observation is in contrast to the polarization selectivity of photomodification experiments at the visible or near infrared ranges [25,26]. The experiments with the planar films photomodification [27] show much worse selectivity in the mid-IR relative to the Vis/near-IR. This fact indicates a larger overlap for the linear polarized plasmon modes at the longer wavelength.
- The experiments in this work were done with the fractal shells on spherical microspheres, which makes polarization selectivity negligible relative to the planar films due to variation in the angle of incidence on the spherical surface.
- A little bit more pronounced difference appeared after the second pulse, which polarization is orthogonal to the first one. The second pulse with orthogonal polarization does not rebuilt the symmetry since the two modes for two polarizations are not independent. Since the process of cross-polarization photoburning is done in series and next step is dependent on the changes made by the previous pulse then the difference in the probe spectra for orthogonal polarizations can be expected.
- We should mention nevertheless, that two pulses with orthogonal polarizations makes better filter contrast than two pulses of the same polarization. The cross polarization photomodification resulted in more than three times decrease of the core-shells' extinction for wavelengths longer than $10.6 \mu\text{m}$. The extinction spectral selectivity and contrast ratio of core-shell structures are comparable to those obtained for planar fractal silver films photomodified

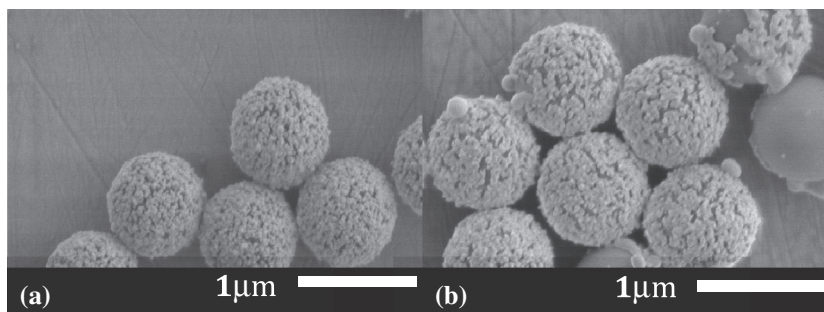


Fig. 8. FESEM images of gold coated SiO_2 microsphere structures. (a) Before and (b) after photomodification with CO_2 pulsed laser.

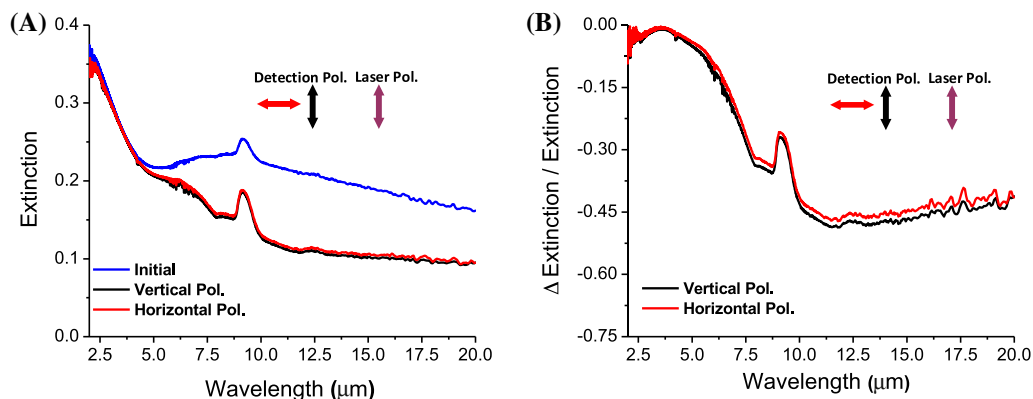


Fig. 9. (A) Extinction (normalized per ZnSe substrate) of the gold coated SiO₂ microsphere structures before (blue) and after photomodification with the CO₂ laser operating at 10.6 μm, (black) vertical and (red) horizontal measurement polarizations, and (B) relative changes in extinction normalized by initial extinction. The laser wavelength was 10.6 μm and energy density was 150 mJ cm⁻². (For interpretation of the references to colour in this figure legend, the reader is referred to the web version of this article.)

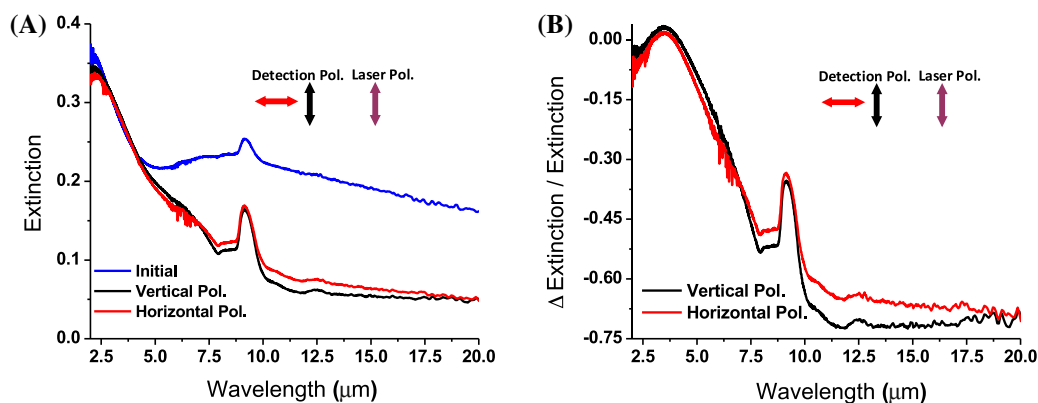


Fig. 10. (A) Extinction (normalized per ZnSe substrate) of the gold coated SiO₂ microsphere structures before (blue) and after photomodification with the CO₂ laser, (black) vertical and (red) horizontal measurement polarizations, and (B) relative changes in extinction normalized by initial extinction. The laser wavelength 10.6 μm and energy density was 150 mJ cm⁻². (For interpretation of the references to colour in this figure legend, the reader is referred to the web version of this article.)

with nanosecond CO₂ laser pulses with energy density of the same order [27] and those theoretically predicted [28].

4. Conclusion

We performed experimental optimization of the mass extinction coefficient for plasmonic core-shell obscurants covering the spectral range from the visible to far-IR due to fractal structure of the shell. The shell gold nanoparticles have been synthesized with the colloidal chemistry method and form fractal nanostructures grown on precipitated calcium carbonate microparticles or silica microspheres. Gold was selected as a more stable shell relative to silver. One can see that mass normalized extinction spectra can be increased by carefully changing the chemical synthesis procedures and the core materials. Gradually increasing the mass of fractal shell the optimal of MEC can be achieved in the whole spectral range of interest. Further increase in the metal coverage results in a transition of the fractal shell to a continuous shell with narrow resonance and increased mass. Among the three samples with silica spherical core of 0.8, 1.8, and 4.5 μm in diameter the optimum in the MEC appeared to be for the 1.8 μm core-shells. Qualitatively it can be explained as a trade of between necessity to provide enough surface area to place enough nanoparticles in the fractal structure to support the plasmon modes at long wavelength range and demand to minimize volume/mass. By etching the silica core the hollow gold shells with good stability and increased mass normalized extinction have been synthesized. The mass normalized

extinction cross section of up to 3 m²/g has been demonstrated in the broad spectral range from the visible to mid-infrared for precipitated calcium carbonate core microparticles. The MEC for PCC is about 4.7 times greater relative to silica, which, in part, is due to the factor 3.3 lower material density and the rest is due to the rich PCC microparticle shape. It is important that the broadband response is a characteristic feature of each core-shell microparticle. The spectral photoburning of resonant areas in the gold fractal shells with CO₂ nanosecond laser resulted in the spectrally selective modification of their extinction. The photomodification resulted in localized and non-uniform changes of gold fractal nanostructures. This led to the formation of obscurants with a window of transparency in the longer wavelength part of the infrared.

Acknowledgement

The authors thank V.M. Shalaev for useful discussions. This work was supported by the Edgewood Chemical Biological Center, United States (the U.S. Army Research Office Scientific Services Program). PN thanks for support by the Polish Ministry of Science and Higher Education grant OR00005408.

References

- [1] J. Owrutsky, et al., Obscurants for infrared countermeasures III, DTIC Document, 2001.

- [2] X. Huang et al., Cancer cell imaging and photothermal therapy in the near-infrared region by using gold nanorods, *J. Am. Chem. Soc.* 128 (6) (2006) 2115–2120.
- [3] O. Neumann et al., Compact solar autoclave based on steam generation using broadband light-harvesting nanoparticles, *Proc. Natl. Acad. Sci.* 110 (29) (2013) 11677–11681.
- [4] S.J. Oldenburg et al., Surface enhanced Raman scattering in the near infrared using metal nanoshell substrates, *J. Chem. Phys.* 111 (10) (1999) 4729–4735.
- [5] S. Katz, A. Snelson, R. Farlow, R. Welker, S. Mainer, Physical and chemical characterization of fog oil smoke and hexachloroethane smoke, in: *Ammunition and Explosives*, IIT RESEARCH INST CHICAGO IL; 1980.
- [6] J.T. Hanley, B.J. Wattle, E.J. Mack, Extinction Characteristics of Pyrotechnically-Generated Alkali-Halide Smokes, Calspan Corporation, Buffalo, NY, 1981.
- [7] M.E. Milham, D.H. Anderson, R.H. Frickel, Infrared optical properties of phosphorus-derived smoke, *Appl. Opt.* 21 (14) (1982) 2501–2507.
- [8] G. Gautam et al., Radiometric screening of red phosphorus smoke for its obscuration characteristics, *Defence Sci. J.* 56 (3) (2006) 377.
- [9] S.H. Oldenburg, A. John, Surface Modified TiO₂ Obscurants for Increased Safety and Performance in Optical Countermeasures Pyrotechnics, Nanocomposix Inc., San Diego, CA, 2012.
- [10] S. Cudziło, A. Papliński, An Influence of the chemical structure of smoke-generating mixtures on laser radiation attenuation at 1.06- μ m and 10.6- μ m wavelengths, *Propellants, Explos., Pyrotech.* 24 (4) (1999) 242–245.
- [11] N.R. Council, Toxicity of Military Smokes and Obscurants, vol. 1, The National Academies Press, Washington, DC, 1997.
- [12] J. Owruisky, et al., Obscurants for infrared countermeasures II, DTIC Document, 2000.
- [13] B.G. DeLacy, D.R. Redding, J. Matthews, Optical, physical, and chemical properties of surface modified titanium dioxide powders, DTIC Document, 2011.
- [14] P.G. Appleyard, N. Davies, Calculation and measurement of infrared mass extinction coefficients of selected ionic and partially ionic insulators and semiconductors: a guide for infrared obscuration applications, *Opt. Eng.* 43 (2) (2004) 376–386.
- [15] N.R. Council, Toxicity of Military Smokes and Obscurants, vol. 2, The National Academies Press, Washington, DC, 1999.
- [16] Graphite, MSDS - Graphite Powder, N. 319.00, Editor. Columbus Chemical Industries Inc, Columbus, WI 53925, 2009.
- [17] C.W. Bruce, S. Alyones, Extinction efficiencies for metallic fibers in the infrared, *Appl. Opt.* 48 (27) (2009) 5095–5098.
- [18] S. Alyones, C.W. Bruce, Electromagnetic scattering and absorption by randomly oriented fibers, *JOSA A* 32 (6) (2015) 1101–1108.
- [19] R. Voss, R. Laibowitz, E. Alessandrini, Fractal (scaling) clusters in thin gold films near the percolation threshold, *Phys. Rev. Lett.* 49 (19) (1982) 1441.
- [20] P. Gadenne, Y. Yagil, G. Deutscher, Transmittance and reflectance insitu measurements of semicontinuous gold films during deposition, *J. Appl. Phys.* 66 (7) (1989) 3019–3025.
- [21] Y. Yagil et al., Optical properties of thin semicontinuous gold films over a wavelength range of 2.5–500 μ m, *Phys. Rev. B* 46 (4) (1992) 2503.
- [22] M.I. Stockman et al., Optical absorption and localization of eigenmodes in disordered clusters, *Phys. Rev. B* 51 (1) (1995) 185.
- [23] M.D. Thoreson et al., Fabrication and realistic modeling of three-dimensional metal-dielectric composites, *J. Nanophotonics* 5 (1) (2011). 051513–051513-17.
- [24] A.K. Sarychev, V.M. Shalaev, *Electrodynamics of Metamaterials*, World Scientific, 2007.
- [25] A. Karpov et al., Observation of a wavelength-and polarization-selective photomodification of silver clusters, *JETP Lett.* 48 (10) (1988) 571. http://www.jetpletters.ac.ru/ps/1110/article_16785.pdf.
- [26] V.P. Safonov et al., Spectral dependence of selective photomodification in fractal aggregates of colloidal particles, *Phys. Rev. Lett.* 80 (5) (1998) 1102–1105.
- [27] P. Nyga et al., Mid-IR plasmonics and photomodification with Ag films, *Appl. Phys. B* 93 (1) (2008) 59–68.
- [28] D.A. Genov, A.K. Sarychev, V.M. Shalaev, Metal-dielectric composite filters with controlled spectral windows of transparency, *J. Nonlinear Opt. Phys. Mater.* 12 (04) (2003) 419–440.
- [29] A.L. Aden, M. Kerker, Scattering of electromagnetic waves from two concentric spheres, *J. Appl. Phys.* 22 (10) (1951) 1242–1246.
- [30] M. Kerker, Invisible bodies, *J. Opt. Soc. Am.* 65 (4) (1975) 376–379.
- [31] H. Chew, M. Kerker, Abnormally low electromagnetic scattering cross sections, *J. Opt. Soc. Am.* 66 (5) (1976) 445–449.
- [32] S. Oldenburg et al., Nanoengineering of optical resonances, *Chem. Phys. Lett.* 288 (2) (1998) 243–247.
- [33] C.A. Rohde, K. Hasegawa, M. Deutsch, Coherent light scattering from semicontinuous silver nanoshells near the percolation threshold, *Phys. Rev. Lett.* 96 (4) (2006) 045503.
- [34] V.C. de Silva, P. Nyga, V.P. Drachev, Scattering suppression in epsilon-near-zero plasmonic fractal shells, *Opt. Mater. Exp.* 5 (11) (2015) 2491–2500.
- [35] T. Pham et al., Preparation and characterization of gold nanoshells coated with self-assembled monolayers, *Langmuir* 18 (12) (2002) 4915–4920.
- [36] S.J. Oldenburg et al., Infrared extinction properties of gold nanoshells, *Appl. Phys. Lett.* 75 (19) (1999) 2897–2899.
- [37] U. Kreibitz, M. Vollmer, *Optical properties of metal clusters*, 1995.
- [38] S. Grésillon et al., Experimental observation of localized optical excitations in random metal-dielectric films, *Phys. Rev. Lett.* 82 (22) (1999) 4520.
- [39] A.L. Smith, Infrared spectra-structure correlations for organosilicon compounds, *Spectrochim. Acta* 16 (1–2) (1960) 87–105.
- [40] G. Ghosh, Dispersion-equation coefficients for the refractive index and birefringence of calcite and quartz crystals, *Opt. Commun.* 163 (1) (1999) 95–102.
- [41] J.D. Passaretti et al., Application of high-opacity precipitated calcium carbonate, *Tappi J. (USA)* 26 (12) (1993).
- [42] D. Werner, S. Hashimoto, T. Uwada, Remarkable photothermal effect of interband excitation on nanosecond laser-induced reshaping and size reduction of pseudospherical gold nanoparticles in aqueous solution, *Langmuir* 26 (12) (2010) 9956–9963.
- [43] S. Link et al., Laser-induced shape changes of colloidal gold nanorods using femtosecond and nanosecond laser pulses, *J. Phys. Chem. B* 104 (26) (2000) 6152–6163.
- [44] C.J. DeSantis et al., Laser-induced spectral hole-burning through a broadband distribution of Au nanorods, *J. Phys. Chem. C* (2015), <http://dx.doi.org/10.1021/acs.jpcc.5b08290>.
- [45] H. Petrova et al., On the temperature stability of gold nanorods: comparison between thermal and ultrafast laser-induced heating, *Phys. Chem. Chem. Phys.* 8 (7) (2006) 814–821.
- [46] C.M. Aguirre et al., Laser-induced reshaping of metallodielectric nanoshells under femtosecond and nanosecond plasmon resonant illumination, *J. Phys. Chem. B* 108 (22) (2004) 7040–7045.
- [47] D. Wan et al., One-shot deep-UV pulsed-laser-induced photomodification of hollow metal nanoparticles for high-density data storage on flexible substrates, *ACS Nano* 4 (1) (2010) 165–173.